NLO QCD corrections to $Zb\bar{b}$ production with massive bottom quarks at the Fermilab Tevatron

F. Febres Cordero[*]

Department of Physics and Astronomy, UCLA, Los Angeles, California 90095-1547, USA

L. Reina[+]

Physics Department, Florida State University, Tallahassee, Florida 32306-4350, USA

D. Wackeroth[‡]

Department of Physics, State University of New York at Buffalo, Buffalo, New York 14260-1500, USA

We calculate the next-to-leading order (NLO) QCD corrections to $Zb\bar{b}$ production in hadronic collisions including full bottom-quark mass effects. We present results for the total cross section and the invariant mass distribution of the bottom-quark jet pair at the Fermilab Tevatron $p\bar{p}$ collider. We perform a detailed comparison with a calculation that considers massless bottom quarks, as implemented in the Monte Carlo program MCFM. We find that neglecting bottom-quark mass effects overestimates the total NLO QCD cross section for $Zb\bar{b}$ production at the Tevatron by about 7%, independent of the choice of the renormalization and factorization scales. Moreover, bottom-quark mass effects can impact the shape of the bottom-quark pair invariant mass distribution, in particular, in the low invariant mass region.

I. INTRODUCTION

One of the main goals of high-energy collider experiments is the elucidation of the mechanism of electroweak symmetry breaking as well as the exploration of energy scales beyond the weak scale, where physics beyond the standard model (SM) is expected. The hadronic production of weak gauge bosons in association with a bottom-quark pair plays a crucial role in some of the current studies of electroweak symmetry breaking and beyond the standard model physics at the Fermilab Tevatron $p\bar{p}$ collider [1–6]. $Wb\bar{b}$ and $Zb\bar{b}$ production processes represent the major irreducible backgrounds to the main search modes for a light SM-like Higgs boson at the Tevatron, i.e. WH and ZH with $H \rightarrow b\bar{b}$. $Wb\bar{b}$ also accounts for one of the most important backgrounds to single-top production, $p\bar{p} \rightarrow t\bar{b}, \bar{t}b$ with $t(\bar{t}) \rightarrow Wb(\bar{b})$, which tests the fundamental structure of the Wtb vertex at the Tevatron [7–10]. Finally, $Zb\bar{b}$ is a background to searches for Higgs bosons in models with enhanced bottom-quark Yukawa couplings, such as the minimal supersymmetric standard model (MSSM) with large $\tan\beta$, where $Hb\bar{b}$ with $H \rightarrow \mu^+\mu^-, \tau^+\tau^-$ is an interesting discovery channel [11].

The hadronic cross sections for W/ZH associated production have been calculated including up to next-to-next-to-leading order QCD corrections [12–14] and $O(\alpha)$ electroweak corrections [15]. Single-top production has been calculated at next-to-leading (NLO) in QCD [16–24], and including one-loop electroweak (SM and MSSM) correc-

tions [25], while the cross section for $Hb\bar{b}$ associated production is known including NLO QCD corrections and full bottom-quark mass effects [26–29].

To fully exploit the Tevatron's potential to detect the SM Higgs boson or to impose limits on its mass, it is crucial that the dominant background processes are also under good theoretical control. In the present experimental analyses,[30] the effects of NLO QCD corrections on the total cross section and the dijet invariant mass distribution of the $W/Zb\bar{b}$ background processes have been taken into account by using the Monte Carlo program MCFM [31]. In MCFM, the NLO QCD predictions of both total and differential cross sections for these processes have been calculated in the zero bottom-quark mass ($m_b = 0$) approximation [32–34], using the analytical results of Refs. [35,36]. From a study of the leading order (LO) cross section, finite bottom-quark mass effects are expected to affect both the total and differential $W/Zb\bar{b}$ cross sections, mostly in the region of small $b\bar{b}$-pair invariant masses [34]. Indeed, since this kinematic region of small $b\bar{b}$-pair invariant masses contributes considerably to $W/Z + nj$ production ($n = 1$, 2), where at least one of the jets is a b-jet, bottom-quark mass effects cannot be neglected as discussed in Refs. [37,38] (for $n = 2$) and in Ref. [39] (for $n = 1$). Given the variety of experimental analyses involved in the search for W/ZH associated production, single-top and $Hb\bar{b}$ production, it is important to assess precisely the impact of a finite bottom-quark mass over the entire kinematical reach of the process, including the complete NLO QCD corrections.

In Ref. [40] we have performed a study of NLO QCD cross sections and invariant mass distributions of the bottom-quark pair in $Wb\bar{b}$ production at the Tevatron,

[*]ffebres@physics.ucla.edu
[+]reina@hep.fsu.edu
[‡]dow@ubpheno.physics.buffalo.edu

including full bottom-quark mass effects. We found that bottom-quark mass effects amount to about 8% of the total NLO cross section at the Tevatron and are mostly visible in the region of low $b\bar{b}$-pair invariant mass.

In this paper, we compute the NLO QCD corrections to $Zb\bar{b}$ hadronic production, including the full bottom-quark mass effects. We consider all partonic processes that contribute at $\mathcal{O}(\alpha\alpha_s^3)$, i.e. NLO QCD corrections to $q\bar{q} \rightarrow Zb\bar{b}$ and $gg \rightarrow Zb\bar{b}$ and the tree-level process $q(\bar{q})g \rightarrow Zb\bar{b}q(\bar{q})$. We present numerical results for the total cross section and the invariant mass distribution of the $b\bar{b}$ pair for the Tevatron $p\bar{p}$ collider, including kinematic cuts and a jet-finding algorithm. In particular, we apply the k_T jet algorithm and require two tagged b-jets in the final state. Using the MCFM package [31], we compare our results with the corresponding results obtained in the $m_b = 0$ limit. Numerical results for both $Zb\bar{b}$ and $Wb\bar{b}$ production at the Large Hadron Collider will be presented in a separate publication [41].

The outline of the paper is as follows. In Sec. II we briefly discuss the technical details of our calculation, while we present numerical results and a discussion of the bottom-quark mass effects in Sec. III. Section IV contains our conclusions.

II. CALCULATION

A. Basics

The total cross section for $p\bar{p}(pp) \rightarrow Zb\bar{b}$ at $\mathcal{O}(\alpha\alpha_s^3)$ can be written as follows:

$$\sigma_{\text{NLO}}(p\bar{p}(pp) \rightarrow Zb\bar{b}) = \sum_{ij} \frac{1}{1 + \delta_{ij}} \int dx_1 dx_2 [\mathcal{F}_i^p(x_1, \mu)$$
$$\times \mathcal{F}_j^{\bar{p}(p)}(x_2, \mu)\hat{\sigma}_{\text{NLO}}^{ij}(x_1, x_2, \mu)$$
$$+ (x_1 \leftrightarrow x_2)], \quad (1)$$

where $\mathcal{F}_i^{p(\bar{p})}$ denote the parton distribution functions (PDFs) for parton i in a proton (antiproton), defined at a generic factorization scale $\mu_f = \mu$. The sum runs over all relevant subprocesses contributing to the hadronic cross section initiated by partons i and j. The partonic cross section for the subprocess $ij \rightarrow Zb\bar{b}(+k)$ is denoted by $\hat{\sigma}_{\text{NLO}}^{ij}$ and is renormalized at an arbitrary scale $\mu_r = \mu$. If not specified otherwise, we assume the factorization and renormalization scales to be equal, $\mu_f = \mu_r = \mu$. The factor in front of the integral is a symmetry factor that accounts for the presence of identical particles in the initial state of a given subprocess (δ_{ij} is the Kronecker delta). The partonic center-of-mass energy squared, s, is given in terms of the hadronic center-of-mass energy squared, s_H, by $s = x_1 x_2 s_H$.

The NLO QCD partonic cross section reads

$$\hat{\sigma}_{\text{NLO}}^{ij}(x_1, x_2, \mu) = \hat{\sigma}_{\text{LO}}^{ij}(x_1, x_2, \mu) + \delta\hat{\sigma}_{\text{NLO}}^{ij}(x_1, x_2, \mu), \quad (2)$$

where $\hat{\sigma}_{\text{LO}}^{ij}(x_1, x_2, \mu)$ denotes the $\mathcal{O}(\alpha\alpha_s^2)$ LO partonic cross section and $\delta\hat{\sigma}_{\text{NLO}}^{ij}(x_1, x_2, \mu)$ describes the $\mathcal{O}(\alpha_s)$ corrections to $\hat{\sigma}_{\text{LO}}^{ij}(x_1, x_2, \mu)$. The LO $p\bar{p}(pp) \rightarrow Zb\bar{b}$ process receives contributions from $q\bar{q}$ and gg initiated processes, as shown in Figs. 1 and 2, respectively. The NLO QCD corrections, $\delta\hat{\sigma}_{\text{NLO}}^{ij}$, receive contributions from $q\bar{q}$, gg, qg, and $\bar{q}g$ initiated processes and can be decomposed in the following way:

$$\delta\hat{\sigma}_{\text{NLO}}^{ij} = \int d(PS_3)\overline{\sum}|\mathcal{A}_{\text{virt}}(ij \rightarrow Zb\bar{b})|^2$$
$$+ \int d(PS_4)\overline{\sum}|\mathcal{A}_{\text{real}}(ij \rightarrow Zb\bar{b} + k)|^2$$
$$\equiv \hat{\sigma}_{\text{virt}}^{ij} + \hat{\sigma}_{\text{real}}^{ij}, \quad (3)$$

where the term integrated over the phase space measure $d(PS_3)$ corresponds to the virtual one-loop corrections with three particles in the final state, while the one integrated over the phase space measure $d(PS_4)$ corresponds to the real tree-level corrections with one additional emitted parton. The sum $\overline{\sum}$ indicates that the corresponding amplitudes squared, $|\mathcal{A}_{\text{virt(real)}}(ij \rightarrow Zb\bar{b}(+k))|^2$, have been averaged over the initial-state degrees of freedom and summed over the final-state ones. The phase space integration has been performed using Monte Carlo (MC) techniques using the adaptive multidimensional integration routine VEGAS [42].

We have improved on the massless calculation of Refs. [33,34] by considering a fully massive b-quark both at the level of the scattering amplitude and in the integration over the phase space of the final-state particles. We keep the Z boson on shell, though the extension to include its leptonic decays does not present in principle any special complications. Because of the complexity of this calculation, all results have been cross-checked with at least two independent sets of codes. The analytic calculation of the scattering amplitudes has been implemented using, at different stages, FORM [43], TRACER [44], MATHEMATICA and MAPLE. Final numerical results have been obtained with codes built in C and FORTRAN, and we
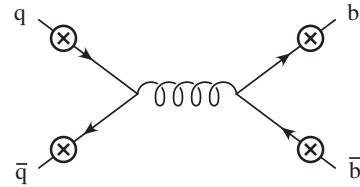

FIG. 1. Tree-level Feynman diagrams for $q\bar{q} \rightarrow Zb\bar{b}$. The circled crosses indicate all possible insertions of the final-state Z boson leg, each insertion corresponding to a different diagram.
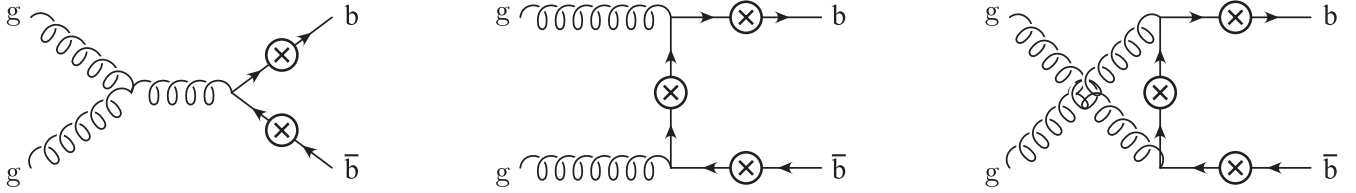
FIG. 2.　Tree-level Feynman diagrams for $gg \rightarrow Zb\bar{b}$. The circled crosses indicate all possible insertions of the final-state Z boson leg, each insertion corresponding to a different diagram.

have used the FF [45] and MADGRAPH [46–48] packages for cross-checks.

The $\mathcal{O}(\alpha_s)$ corrections to $Zb\bar{b}$ production are similar in structure to the NLO QCD corrections to $Wb\bar{b}$ production [40] and to Higgs production in association with top quarks ($Ht\bar{t}$) [49,50]. We therefore only summarize below the most important features of the calculation and refer to the $Wb\bar{b}$ and $Ht\bar{t}$ papers cited above and to Ref. [51] for more details. The $\mathcal{O}(\alpha_s)$ corrections to $q\bar{q} \rightarrow Zb\bar{b}$ can be derived from the $\mathcal{O}(\alpha_s)$ corrections to $q\bar{q}' \rightarrow Wb\bar{b}$ production [40] (with $W \leftrightarrow Z$) and to $q\bar{q} \rightarrow Ht\bar{t}$ [49] (with $t \leftrightarrow b$ and $H \leftrightarrow Z$), while the $\mathcal{O}(\alpha_s)$ corrections to the gg initiated $Zb\bar{b}$ production process can be obtained from the $\mathcal{O}(\alpha_s)$ corrections to $gg \rightarrow Ht\bar{t}$ [50] (with $t \leftrightarrow b$ and $H \leftrightarrow Z$). The qg, $\bar{q}g$ initiated processes appear in both $Wb\bar{b}$ and $Ht\bar{t}$ NLO QCD calculations with $W \leftrightarrow Z$ and $H \leftrightarrow Z$, $t \leftrightarrow b$, respectively. Note that, when applying the results of $Wb\bar{b}$ and $Ht\bar{t}$ production of Refs. [40,49,50], one also needs to replace, respectively, the Wff' and fermion Yukawa couplings by the $V - A$ coupling of fermions to the Z boson:

$$\text{(diagram)} = \frac{-ie}{2\sin\theta_W\cos\theta_W}\gamma^\mu(g_V^f - g_A^f\gamma_5)\,, \quad (4)$$

where θ_W is the weak mixing angle and the vector, g_V^f, and axial-vector, g_A^f, couplings for the Zff vertex are given by

$$g_V^f = T_3^f - 2\sin^2\theta_W Q_f, \qquad g_A^f = T_3^f, \quad (5)$$

with T_3^f denoting the third component of the weak isospin and Q_f the electric charge of the fermion f. Moreover, as we are considering an on-shell Z boson, we have summed over its polarizations as follows:

$$\sum \epsilon^\mu(p_Z)\epsilon^{\nu*}(p_Z) = -g^{\mu\nu} + \frac{p_Z^\mu p_Z^\nu}{M_Z^2}, \quad (6)$$

where M_Z is the mass of the Z boson.

B. The virtual cross section $\hat{\sigma}_{\text{virt}}^{ij}$

The $\mathcal{O}(\alpha_s)$ virtual corrections to the partonic tree-level $q\bar{q} \rightarrow Zb\bar{b}$ and $gg \rightarrow Zb\bar{b}$ production processes consist of self-energy, vertex, box, and pentagon diagrams, as shown,

for the $Ht\bar{t}$-like part, in Figs. 2–4 of Ref. [49] and Figs. 2–5 of Ref. [50], respectively (for a full set of diagrams see also Ref. [51]). The contributions to $\hat{\sigma}_{ij}^{\text{virt}}$ in Eq. (3) can be written as

$$\overline{\sum}|\mathcal{A}_{\text{virt}}(ij \rightarrow Zb\bar{b})|^2 = \sum_D \overline{\sum}(\mathcal{A}_0\mathcal{A}_D^\dagger + \mathcal{A}_0^\dagger\mathcal{A}_D)$$
$$= \sum_D \overline{\sum} 2\,\mathcal{R}e(\mathcal{A}_0\mathcal{A}_D^\dagger), \quad (7)$$

where $\mathcal{A}_0$ is the tree-level amplitude and $\mathcal{A}_D$ denotes the amplitude for the one-loop diagram D, with D running over all self-energy, vertex, box, and pentagon diagrams corresponding to the ij-initiated subprocess.

The calculation of each virtual diagram ($\mathcal{A}_D$) is performed in the same way as outlined in Refs. [49,50], i.e. $\mathcal{A}_D$ is calculated as a linear combination of Dirac structures with coefficients that depend on both scalar and tensor one-loop Feynman integrals with up to five denominators. We solve the one-loop integrals in the coefficients either at the level of the amplitude or at the level of the amplitude squared [see Eq. (7)]. These two independent approaches allow us to thoroughly cross-check the calculation of each individual diagram. Indeed, the tensor structures present in the one-loop integrals of the amplitude are typically different from the ones present in the amplitude squared, as one can perform nontrivial reductions of the latter by canceling dot-products of the integration momentum in the numerator with denominators in the Feynman integrals. In this way, the final analytical expression of a given diagram ends up being represented in terms of different building blocks. A possible incorrect relation between the building blocks would then naturally produce a discrepancy between the two approaches.

Tensor and scalar one-loop integrals are treated as follows. Using the Passarino-Veltman (PV) method [52,53], the tensor integrals are expressed as a linear combination of tensor structures and coefficients, where the tensor structures depend on the external momenta and the metric tensor, while the coefficients depend on scalar integrals, kinematics invariants, and the dimension of the integral. Numerical stability issues may arise at this level as a consequence of the proportionality of the tensor integral coefficients to powers of inverse Gram determinants (GDs), as discussed in detail in Ref. [50], although for $Zb\bar{b}$ production the problem is considerably more serious.

These numerical instabilities can be considered as "spurious" or "unphysical" divergences, since it is well known that only two-particle invariants can give rise to a physical singularity. Indeed, these spurious divergences cancel when large sets of diagrams are combined [36], such as, for example, when one combines gauge invariant sets of color amplitudes (i.e. amplitudes with a common color factor). As we have expressed our calculation in terms of invariants, and we employ a standard basis of scalar integrals, the full cancellation only occurs between numerator and denominator at the numerical level, often between fairly large expressions.

For this reason we have chosen to organize the diagrams, at certain stages, into gauge invariant color amplitudes, that is, into coefficients of the same color structure (see Ref. [51]). This allows a better handling of the spurious singularities and a natural way to make internal cross-checks and cross-checks with new techniques. When we consider these gauge invariant sets of color amplitudes and full analytical reductions of all tensor integrals, we find cancellation of some powers of GDs, which improves the numerical stability of our code, so that when integrating over the $Zb\bar{b}$ phase space, using MC techniques, we obtain statistical errors below 0.1% for total cross sections.

The fully reduced numerical codes are often more demanding computationally, and because of that we have built master codes that use them only when close to regions of phase space where certain problematic GDs become small. All this is found particularly useful when considering higher rank D-PV functions (we have up to $D4$-PV functions in our calculation) as well as E-PV functions. This technique would probably break down if one were to extend it to processes with even more legs, and the use of helicity amplitudes would in this case be preferable.

In the case of pentagon diagrams, a powerful and convenient check consists of reducing consistently all E-PV functions by canceling systematically, at the level of the amplitude squared in Eq. (7), all possible vector products containing the loop momentum in the numerator with some denominators. This is possible as, in the pentagon topology of our process, each leg has an outgoing momentum which is on shell, corresponding basically to one of the external initial or final particles of the subprocess. One then ends with expressions for each pentagon diagram containing purely scalar pentagon integrals, or tensor integrals with fewer than five denominators, improving considerably the numerical stability. We compared analytically these reductions to the nonreduced expressions by using the full reduction of all tensor integrals to scalar integrals, and found agreement.

We also checked parts of our result by using unitarity techniques [36], specifically the quadruple-cut technique [54]. As shown by Britto, Cachazo, and Feng, from any set of Feynman diagrams (or more generally from any tensor integral [55]) one can extract the coefficient of a given

scalar box integral by cutting the four corresponding propagators (see Fig. 3), i.e. by replacing $i/(p^2 - m^2 + i\epsilon) \rightarrow 2\pi\delta^{(+)}(p^2 - m^2)$ for each cut propagator of momentum p and mass m. This effectively freezes the momentum integration and replaces it by a set of algebraic equations which determine the loop momentum entirely. We solved this set of equations by using a Britto-Cachazo-Feng ansatz [54], and then compared the result to the corresponding box coefficient extracted from our analytic expression, and found agreement (for more details and specific solutions for the topology in Fig. 3 see Ref. [51]). This is a rather nontrivial check for the set of E-PV and D-PV functions we have employed at different stages, since they all contribute to the coefficients of the scalar D-functions occurring in the one-loop $Zb\bar{b}$ amplitude. For instance, it has been particularly useful in the case of box diagrams like the one shown in Fig. 3, since this diagram and related ones contain up to $D4$-PV functions that cannot be reduced even at the level of the amplitude squared. Since they involve up to four powers of inverse GDs, they are particularly subject to numerical instabilities and it is important to have their analytic expressions as compact as possible.

After the tensor integral reduction is performed, the fundamental building blocks are one-loop scalar integrals with up to five denominators. They may be finite or contain both ultraviolet (UV) and infrared (IR) divergences. The finite scalar integrals are evaluated using the method described in Ref. [53] and cross-checked with the numerical package FF [45]. The UV and IR singular scalar integrals are calculated analytically by using dimensional regularization in $d = 4 - 2\epsilon$ dimensions. The most difficult integrals arise from IR-divergent pentagon diagrams with several external and internal massive particles. We calculate them as linear combinations of box integrals using the method of Refs. [56,57] and of Ref. [53]. Details of the box scalar integrals (see also Ref. [58]) and the pentagon reduction, as well as the set of IR-divergent three- and
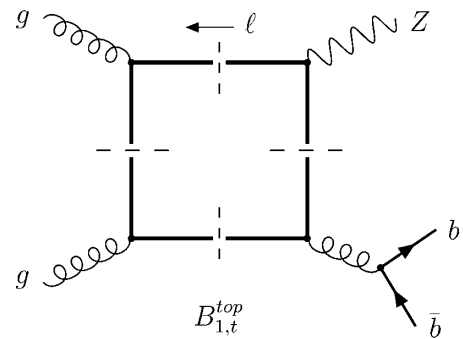

FIG. 3. Quadruple cut [54] check of the calculation of a box diagram involving a top-quark loop. It corresponds to two Feynman diagrams given by the two possible orientations of the fermion line.

two-point functions used in this calculation, are given in Ref. [51].

The UV singularities of the virtual cross section are removed by introducing a suitable set of counterterms (see Refs. [49–51] for details), while the residual renormalization scale dependence is checked from first principles using renormalization group arguments as in Eq. (4) of Ref. [50]. Note that we use the on-shell subtraction scheme when fixing the wave function renormalization constant of the external bottom-quark field ($\delta Z_2^{(b)}$) and the mass renormalization constant (δm_b). The IR singularities of the virtual cross section are canceled by analogous singularities in the $\mathcal{O}(\alpha\alpha_s^3)$ real cross section.

In our calculation we treat γ_5 according to the naive dimensional regularization approach, i.e. we enforce the fact that γ_5 anticommutes with all other γ matrices in $d = 4 - 2\epsilon$ dimensions. This is known to give rise to inconsistencies when, at the same time, the d-dimensional trace of four γ matrices and one γ_5 is forced to be nonzero [as in $d = 4$, where $\text{Tr}(\gamma^\mu\gamma^\nu\gamma^\rho\gamma^\sigma\gamma_5) = 4i\epsilon^{\mu\nu\rho\sigma}$] [59]. In our calculation, both UV and IR divergences are handled in such a way that we never have to enforce simultaneously these two properties of the Dirac algebra in d dimensions. For instance, the UV divergences are extracted and canceled at the amplitude level, after which the $d \rightarrow 4$ limit is taken and the renormalized amplitude is squared using $d = 4$. Thus, all fermion traces appearing at this point are computed in four dimensions and therefore have no ambiguities.

We note that the tree-level amplitude $\mathcal{A}_0$ in Eq. (7) has generically to be considered as a d-dimensional tree-level amplitude. This matters when the $\mathcal{A}_D$ amplitudes in Eq. (7) are UV or IR divergent. Actually, as it has been shown in Refs. [49,50], both UV and IR divergences are always proportional to the tree-level amplitudes and they can be formally canceled without having to explicitly specify the dimensionality of the tree-level amplitude itself. After UV and IR singularities have been canceled, the remaining phase space integration is computed in $d = 4$ dimensions using standard MC techniques.

C. The real cross section $\hat{\sigma}_{\text{real}}^{ij}$

The NLO QCD real cross section $\hat{\sigma}_{\text{real}}^{ij}$ in Eq. (3) corresponds to the $\mathcal{O}(\alpha_s)$ corrections to $ij \rightarrow Zb\bar{b}$ due to the emission of an additional real parton, i.e. to the process $ij \rightarrow Zb\bar{b} + g$, and the tree-level process $q(\bar{q})g \rightarrow Zb\bar{b} + q(\bar{q})$. $\hat{\sigma}_{\text{real}}^{ij}$ contains IR singularities which cancel the analogous singularities present in the $\mathcal{O}(\alpha_s)$ virtual corrections and in the NLO PDFs (see Refs. [49–51] for details). These singularities can be either *soft*, when the emitted extra parton is a gluon and its energy becomes very small, or *collinear*, when the final-state parton is emitted collinear to one of the partons in the initial state. There is no collinear singularity arising from the radiation off the final-state bottom quarks, since they are considered to be massive.

We have calculated the cross sections for the processes

$$i(q_1) + j(q_2) \rightarrow b(p_b) + \bar{b}(p_{\bar{b}}) + Z(p_Z) + g(k)$$

and

$$(q, \bar{q})(q_1) + g(q_2) \rightarrow b(p_b) + \bar{b}(p_{\bar{b}}) + Z(p_Z) + (q, \bar{q})(k),$$

with $q_1 + q_2 = p_b + p_{\bar{b}} + p_Z + k$, using the *two-cutoff* phase space slicing (PSS) method. This implementation of the PSS method was originally developed to study QCD corrections to dihadron production [60] and has since then been applied to a variety of processes (a nice review can be found in Ref. [61]). We follow closely the application of the PSS method to $Ht\bar{t}$ production as presented in Refs. [49,50] to which we refer for more extensive references and full details. Although we are considering $Zb\bar{b}$ production, the kinematics are equivalent, and the color structure and IR behavior are the same, so necessarily their soft and collinear kernels are the same. In the following we briefly summarize our implementation of the *two-cutoff* PSS method.

Using the PSS method, the IR singularities can be conveniently isolated by *slicing* the phase space of the final-state particles into different regions defined by suitable cutoffs. To isolate the soft and collinear singularities we impose soft (δ_s) and collinear (δ_c) cutoffs on the phase space of the emitted parton as follows. By introducing an arbitrary small *soft* cutoff δ_s, we separate the overall integration of the $q\bar{q}, gg \rightarrow b\bar{b}Z + g$ phase space into two regions according to whether the energy of the final-state gluon ($k^0 = E_g$) is *soft*, i.e. $E_g \leq \delta_s\sqrt{s}/2$, or *hard*, i.e. $E_g > \delta_s\sqrt{s}/2$. In order to isolate the collinear singularities, we further divide the hard region of the $q\bar{q}, gg \rightarrow b\bar{b}Z + g$ phase space into a *hard/collinear* and a *hard/noncollinear* region, by introducing a second small *collinear* cutoff δ_c. The *hard/noncollinear* region is defined by the condition that both

$$\frac{2q_1 \cdot k}{E_g\sqrt{s}} > \delta_c \quad \text{and} \quad \frac{2q_2 \cdot k}{E_g\sqrt{s}} > \delta_c \qquad (8)$$

are true. We apply the same collinear cutoff to the tree-level process $q(\bar{q})g \rightarrow Zb\bar{b} + q(\bar{q})$. The hard noncollinear parts of the real cross sections, $\hat{\sigma}_{\text{hard/noncoll}}^{q\bar{q},gg,qg}$, are finite and can be computed numerically. The partonic real cross sections can then be written as follows:

$$\hat{\sigma}_{\text{real}}^{q\bar{q},gg,qg} = \hat{\sigma}_{\text{soft}}^{q\bar{q},gg} + \hat{\sigma}_{\text{hard/coll}}^{q\bar{q},gg,qg} + \hat{\sigma}_{\text{hard/noncoll}}^{q\bar{q},gg,qg}, \qquad (9)$$

where $\hat{\sigma}_{\text{soft}}^{q\bar{q},gg}$ and $\hat{\sigma}_{\text{hard/coll}}^{q\bar{q},gg,qg}$ are obtained by integrating analytically over the *soft* and *collinear* regions of the phase space of the emitted parton, respectively, and contain all the IR divergences of $\hat{\sigma}_{\text{real}}^{q\bar{q},gg,qg}$. The dependence on these

arbitrary cutoffs, δ_s, δ_c, is not physical and cancels at the level of the real cross section, i.e. in $\hat{\sigma}^{ij}_{\text{real}}$. This cancellation constitutes an important check of the calculation.

We conclude this section by showing explicitly that the total hadronic cross section at NLO QCD does not depend on the arbitrary cutoffs introduced by the PSS method, i.e. on δ_s and δ_c. The cancellation of the PSS cutoff dependence is realized in $\hat{\sigma}^{ij}_{\text{real}}$ by matching contributions that are calculated either analytically ($\hat{\sigma}^{ij}_{\text{soft}}$ and $\hat{\sigma}^{ij}_{\text{hard/coll}}$), in the IR-unsafe region below the cutoffs, or numerically, in the IR-safe region above the cutoffs ($\hat{\sigma}^{ij}_{\text{hard/noncoll}}$). While the analytical calculation in the IR-unsafe region reproduces the form of the cross section in the soft or collinear limits and is therefore only accurate for small values of the cut-offs, the numerical integration in the IR-safe region becomes unstable for very small values of the cutoffs. Therefore, obtaining a convincing cutoff independence involves a delicate balance between the previous antago-nistic requirements and ultimately dictates the choice of values that are neither too large nor too small for the cutoffs. In Figs. 4 and 5 we demonstrate the independence of $\sigma_{\text{NLO}}(p\bar{p} \to Zb\bar{b})$ on δ_s and δ_c separately, by varying only one of the two cutoffs over an extended range, while the other is kept fixed. In Fig. 4, δ_s is varied between 10^{-5} and 10^{-2} with $\delta_c = 10^{-5}$, while in Fig. 5, δ_c is varied between 10^{-7} and 10^{-4} with $\delta_s = 10^{-3}$. In both plots, we show in the upper window the overall cutoff-dependence cancellation between the hadronic cross sections $\sum_{ij}(\sigma^{ij}_{\text{soft}} + \sigma^{ij}_{\text{hard/coll}})$ and $\sum_{ij}\sigma^{ij}_{\text{hard/noncoll}}$ in $\sum_{ij}\sigma^{ij}_{\text{real}}$, in-

FIG. 5 (color online). Dependence of $\sigma_{\text{NLO}}(p\bar{p} \to Zb\bar{b})$ on the collinear cutoff δ_c of the two-cutoff PSS method, for $\mu = 2m_b + M_Z$, and $\delta_s = 10^{-3}$. The upper plot shows the cancella-tion of the δ_s-dependence between $\sigma_{\text{soft}} + \sigma_{\text{hard/coll}}$, and $\sigma_{\text{hard/noncoll}}$. The lower plot shows, on an enlarged scale, the dependence of the full $\sigma_{\text{NLO}} = \sigma^{gg}_{\text{NLO}} + \sigma^{q\bar{q}}_{\text{NLO}} + \sigma^{qg}_{\text{NLO}}$ on δ_c with the corresponding statistical errors of the MC integration.

cluding all channels, gg, $q\bar{q}$, and qg. Note that we also take into account contributions from the LO and the virtual cross sections which are cutoff independent. In the lower window of the same plots we show the full σ_{NLO}, including all channels, on a scale that magnifies the details of the cutoff-dependence cancellation. The statistical errors from the MC phase space integration are also shown. Both Figs. 4 and 5 show a clear plateau over a wide range of δ_s and δ_c and the NLO cross section is proven to be cutoff independent. The numerical results presented in Sec. III have been obtained by using the two-cutoff PSS method with $\delta_s = 10^{-3}$ and $\delta_c = 10^{-5}$.
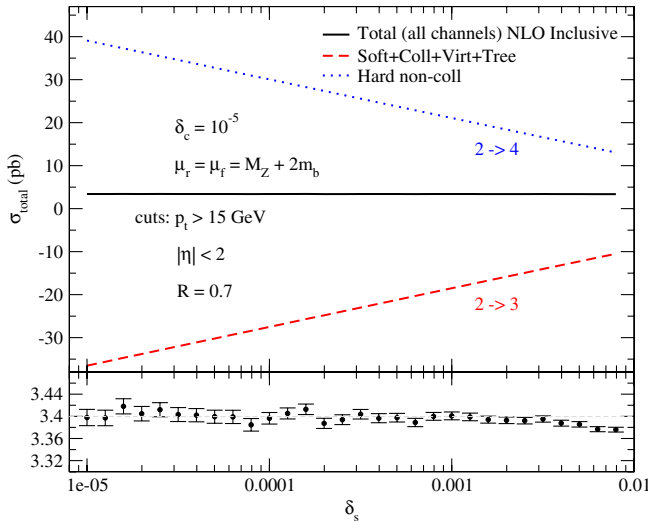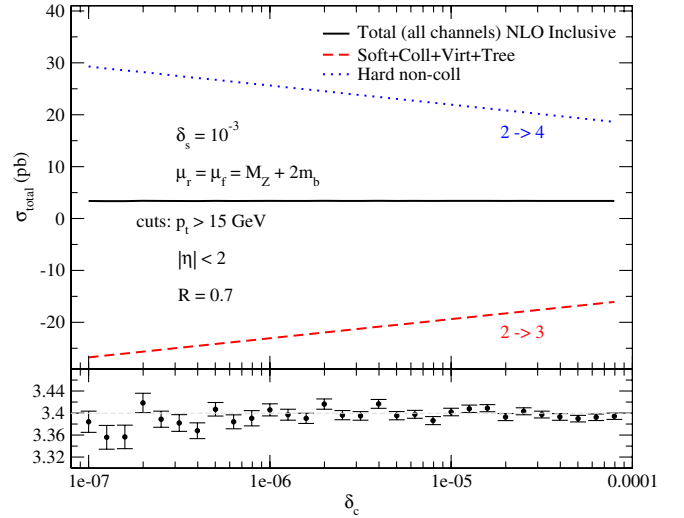

FIG. 4 (color online). Dependence of $\sigma_{\text{NLO}}(p\bar{p} \to Zb\bar{b})$ on the soft cutoff δ_s of the two-cutoff PSS method for $\mu = 2m_b + M_Z$, and $\delta_c = 10^{-5}$. The upper plot shows the cancellation of the δ_s dependence between $\sigma_{\text{soft}} + \sigma_{\text{hard/coll}}$ and $\sigma_{\text{hard/non-coll}}$. The lower plot shows, on an enlarged scale, the dependence of the full $\sigma_{\text{NLO}} = \sigma^{gg}_{\text{NLO}} + \sigma^{q\bar{q}}_{\text{NLO}} + \sigma^{qg}_{\text{NLO}}$ on δ_s with the correspond-ing statistical errors of the MC integration.

III. NUMERICAL RESULTS

The results for $Zb\bar{b}$ observables presented in this paper are obtained for the Tevatron $p\bar{p}$ collider at $s_H = 1.96$ TeV. If not stated otherwise, we assume a nonzero bottom-quark mass, fixed at $m_b = 4.62$ GeV. The mass of the top quark, entering in the virtual corrections, is set to $m_t = 170.9$ GeV. The Z-boson mass is taken to be $M_Z = 91.1876$ GeV [62] and the W-boson mass is calculated from $M_W = M_Z \cos\theta_w$ with $\sin^2\theta_w = 0.223$. We work in the electroweak G_μ input scheme and replace the fine structure constant $\alpha(0) = e^2/(4\pi)$ by $\alpha(G_\mu) = \frac{\sqrt{2}}{\pi} G_\mu M_W^2 \sin^2\theta_w$ with the Fermi constant $G_\mu = 1.16639 \cdot 10^{-5}$ GeV^{-2}. The LO results use the one-loop evolution of α_s and the CTEQ6L1 set of PDFs [63], with $\alpha_s^{LO}(M_Z) = 0.130$, while the NLO results use the two-loop evolution of

α_s and the CTEQ6M set of PDFs, with $\alpha_s^{\mathrm{NLO}}(M_Z) = 0.118$. In the calculation of the parton luminosity we assume five light flavors in the initial state. Including the b-quark PDF has a negligible effect ($< 0.1\%$) on the $Zb\bar{b}$ cross section and is included to consistently compare with MCFM. We implement the k_T jet algorithm [64–67] with a pseudocone size $R = 0.7$ and we recombine the parton momenta within a jet using the so-called covariant E-scheme [65]. We checked that our implementation of the k_T jet algorithm coincides with the one in MCFM. We require all events to have a $b\bar{b}$ jet pair in the final state, with a transverse momentum larger than 15 GeV ($p_T^{b,\bar{b}} > 15$ GeV) and a pseudorapidity that satisfies $|\eta^{b,\bar{b}}| < 2$. We impose the same p_T and $|\eta|$ cuts also on the extra jet that may arise due to hard noncollinear real emission of a parton, i.e. in the processes $Zb\bar{b} + g$ or $Zb\bar{b} + q(\bar{q})$. This hard noncollinear extra parton is treated either *inclusively* or *exclusively*. In the *inclusive* case we include both two- and three-jet events, while in the *exclusive* case we require exactly two jets in the event. Two-jet events consist of a bottom-quark jet pair that may also include a final-state light parton (gluon or quark) due to the applied recombination procedure. Results in the massless bottom-quark approximation have been obtained using the MCFM code [31].

In Table I we present results for the total LO and NLO QCD $p\bar{p} \rightarrow Zb\bar{b}$ cross sections, obtained with the scale $\mu_r = \mu_f = M_Z + 2m_b$, for both our fully massive calculation and in the massless approximation. As can be seen, the NLO QCD corrections increase considerably the total cross section, with NLO vs LO ratios (K-factors) that, in both the massive and massless bottom-quark case, amount to $K = 1.54$ and $K = 1.27$ for the *inclusive* and *exclusive* case, respectively. In the following we will study the impact of the NLO QCD corrections on $Zb\bar{b}$ observables in more detail. Specifically we will show examples of kinematic distributions where a global rescaling (or K-factor) does not properly describe the effect of these corrections.

In Figs. 6 and 7 we illustrate the renormalization and factorization scale dependence of the LO and NLO QCD total cross sections, both in the *inclusive* and *exclusive* case. Figure 6 shows the overall scale dependence of
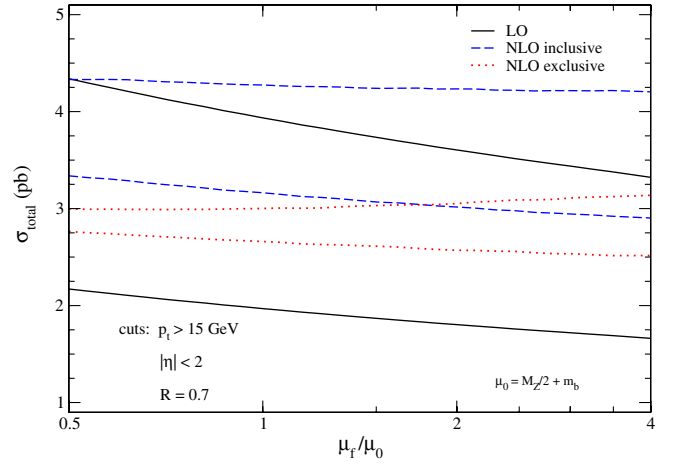

FIG. 6 (color online). Dependence of the LO (black solid band), NLO *inclusive* (blue dashed band), and NLO *exclusive* (red dotted band) $Zb\bar{b}$ total cross sections on the renormalization/factorization scales, including full bottom-quark mass effects. The bands are obtained by independently varying both μ_r and μ_f between $\mu_0/2$ and $4\mu_0$ (with $\mu_0 = m_b + M_Z/2$).

both LO, NLO *inclusive* and NLO *exclusive* total cross sections, when both μ_r and μ_f are varied independently between $\mu_0/2$ and $4\mu_0$ (with $\mu_0 = m_b + M_Z/2$), including full bottom-quark mass effects. We notice that the NLO QCD cross sections have a reduced scale dependence over the range of scales shown, and the *exclusive* NLO QCD cross section is more stable than the *inclusive* one. This effect is mainly driven by the tree-level subprocess $q(\bar{q})g \rightarrow Zb\bar{b} + q(\bar{q})$ contributing to the real corrections. This is illustrated by the right-hand side plots of Figs. 7(a) and 7(b), where we show separately the μ-dependence of the total cross sections to the $q\bar{q}$, $qg + \bar{q}g$, and gg initiated processes, for $\mu_r = \mu_f$, both for the *inclusive* and for the *exclusive* cases. It is clear that the low scale behavior of the *inclusive* cross section is considerably affected by the $qg + \bar{q}g$ contribution, which shows a monotonic dependence on μ (i.e. with no plateau) characteristic of tree-level processes. In the left-hand side plots of Figs. 7(a) and 7(b) we also compare the scale dependence of our results to the scale dependence of the corresponding results obtained with $m_b = 0$ (using MCFM), both at LO and at NLO. Using a nonzero value of m_b is expected to have a small impact on the scale dependence of the results,[1] since the only modification to the renormalization scale dependence originates from the bottom-quark mass and field renormalization, as discussed in Sec. IIB of Ref. [27], where we compare the minimal and on-shell subtraction schemes. Indeed, as can be seen in Figs. 7(a) and 7(b) the scale dependence of the LO and

TABLE I. LO and NLO total $Zb\bar{b}$ cross sections at the Tevatron for massive and massless bottom quarks, using $\mu_r = \mu_f = M_Z + 2m_b$. The numbers in square brackets are the ratios of the NLO and LO cross sections, the so called K-factors. Statistical errors of the MC integration amount to about 0.1%.

Cross section	$m_b \neq 0$ (pb) [ratio]	$m_b = 0$ (pb) [ratio]
σ_{LO}	2.21[−]	2.37[−]
σ_{NLO} *inclusive*	3.40[1.54]	3.64[1.54]
σ_{NLO} *exclusive*	2.80[1.27]	3.01[1.27]

---

[1]Note that we always use $m_b = 4.62$ GeV in the determination of the scales in terms of $\mu_0 = m_b + M_Z/2$ even in the results obtained with $m_b = 0$.
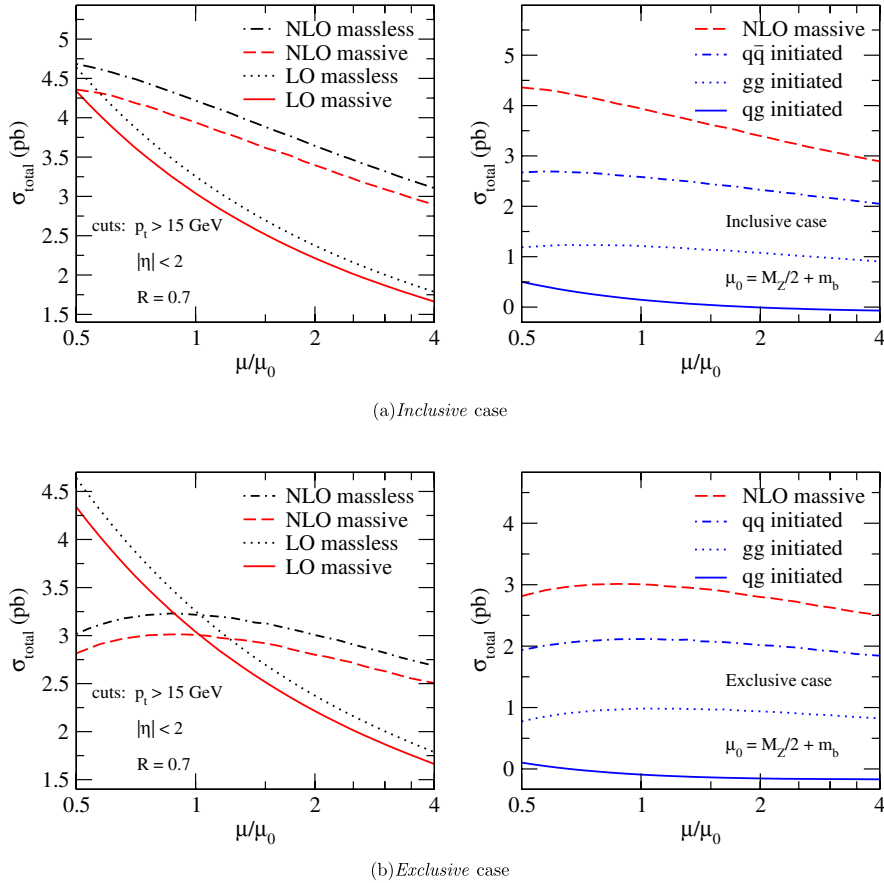
FIG. 7 (color online).   Dependence of the LO and NLO *inclusive* and *exclusive* $Zb\bar{b}$ total cross section on the renormalization/factorization scale, when $\mu_r = \mu_f = \mu$. The left-hand side plots compare both LO and NLO total cross sections for the case in which the bottom quark is treated as massless (MCFM) or massive (our calculation). The right-hand side plots show separately, for the massive case only, the scale dependence of the $q\bar{q}$, gg, and $qg + \bar{q}g$ contributions, as well as their sum.

NLO curves is very similar for both the case of a massive and massless bottom quark. While the LO cross section still has a 45% uncertainty due to scale dependence, this uncertainty is reduced at NLO to about 20% for the *inclusive* and to about 11% for the *exclusive* cross sections. The uncertainties have been estimated as the positive/negative deviation with respect to the midpoint of the bands plotted in Fig. 6, where each band range is defined by the minimum and maximum value in the band. We notice incidentally that the difference in the total cross section due to finite bottom-quark mass effects is less significant than the theoretical uncertainty due to the residual scale dependence in the *inclusive* case, but is comparable in size in the *exclusive* case. Indeed, the finite bottom-quark mass effects amount to a reduction of the total cross sections by about 7% compared to the massless case at both LO and NLO QCD.

In Fig. 8, we show the rescaled difference between the NLO total cross sections obtained from our calculation (with $m_b \neq 0$) and with MCFM (with $m_b = 0$) defined as follows:
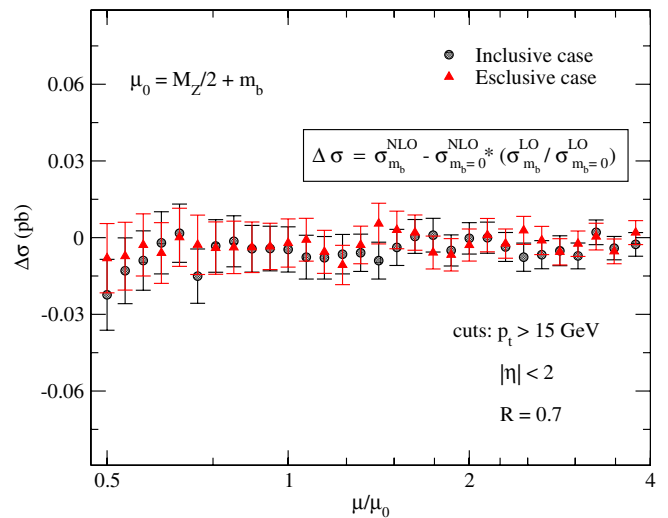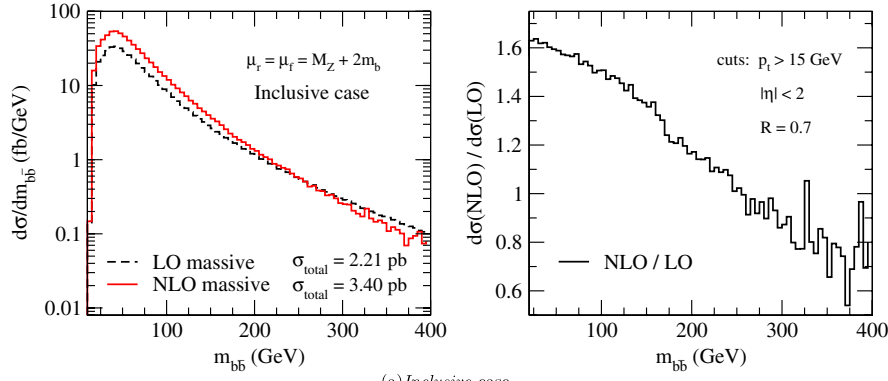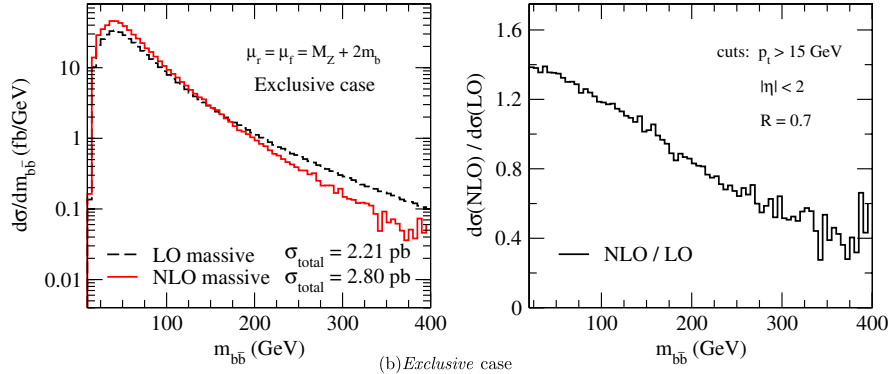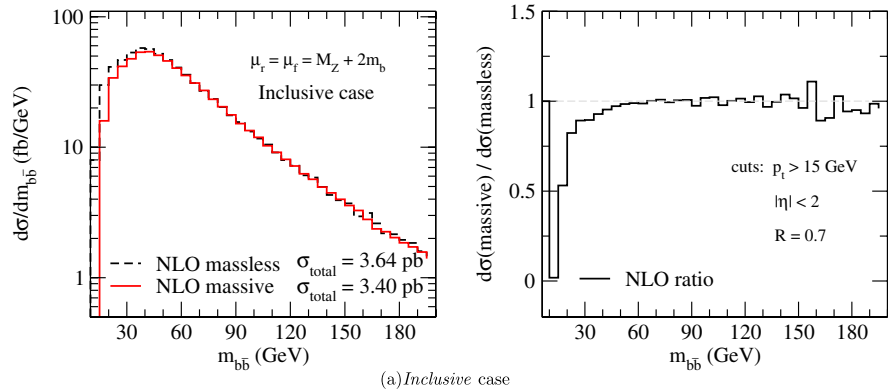

FIG. 8 (color online).   Dependence on the renormalization/factorization scale of the rescaled difference between our NLO calculation (with $m_b \neq 0$) of the $Zb\bar{b}$ total cross section and MCFM (with $m_b = 0$) for the *inclusive* and *exclusive* cases (with $\mu_r = \mu_f$). The error bars indicate the statistical uncertainty of the MC integration.
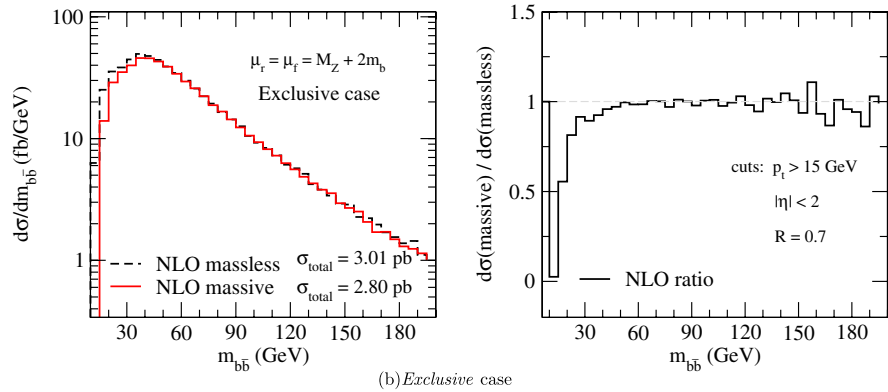
FIG. 9 (color online). The distribution $d\sigma/dm_{b\bar{b}}$ at LO and NLO QCD. The right-hand side plots show the ratio of the LO and NLO distributions.

FIG. 10 (color online). The *inclusive* and *exclusive* NLO QCD distributions $d\sigma/dm_{b\bar{b}}$ derived from our calculation (with $m_b \neq 0$) and from MCFM (with $m_b = 0$). The right-hand side plots show the ratio of the two distributions, $d\sigma(m_b \neq 0)/d\sigma(m_b = 0)$.

$$\Delta\sigma = \sigma^{\text{NLO}}(m_b \neq 0) - \sigma^{\text{NLO}}(m_b = 0)\frac{\sigma^{\text{LO}}(m_b \neq 0)}{\sigma^{\text{LO}}(m_b = 0)}. \tag{10}$$

As can be seen, within the statistical errors of the MC integration, the finite bottom-quark mass effects on the total cross sections at NLO are well described by the corresponding effects at LO.

Finally, in Figs. 9–11 we study the distribution $d\sigma/dm_{b\bar{b}}$, where $m_{b\bar{b}}$ is the invariant mass of the $b\bar{b}$ jet pair. The impact of NLO QCD corrections on this distribution is illustrated in Figs. 9(a) and 9(b) for the *inclusive* and *exclusive* cases, respectively. We see that the NLO QCD corrections affect the differential cross section quite substantially. In each figure the right-hand side plot gives the ratio of the NLO and LO distributions. We stress the fact that the NLO $m_{b\bar{b}}$ distributions cannot be obtained from the LO ones by just rescaling, which is clear from the right-hand side plots of Fig. 9.

Figures 10(a) and 10(b) compare the NLO $d\sigma/dm_{b\bar{b}}$ distributions obtained from the massive and massless bottom-quark calculations. The results with $m_b = 0$ have been obtained using MCFM. As expected, most of the difference between the massless and massive bottom-quark cross sections is coming from the region of low $m_{b\bar{b}}$ invariant mass, both for the *inclusive* and *exclusive* cases, where the cross sections for $m_b \neq 0$ are consistently below the ones with $m_b = 0$. This is emphasized in the right-hand side plots, where we show the ratio of the two distributions, $d\sigma(m_b \neq 0)/d\sigma(m_b = 0)$. For completeness, we also show in Fig. 11 the comparison between massive ($m_b \neq 0$) and massless ($m_b = 0$) calculations at LO in QCD. The LO $m_{b\bar{b}}$ distribution for massive bottom quarks has been obtained both from our calculation and from MCFM, which implements the $m_b \neq 0$ option at tree level, and both results agree perfectly. In general, mass effects are similar at LO and NLO. To illustrate this in more detail we show in Fig. 12 the rescaled difference between the $m_{b\bar{b}}$ distributions obtained with our NLO calculation (with

FIG. 12 (color online). The $m_{b\bar{b}}$ distribution of the rescaled difference between our NLO calculation (with $m_b \neq 0$) and MCFM (with $m_b = 0$) for the *inclusive* (upper plot) and *exclusive* case (lower plot).

$m_b \neq 0$) and with MCFM (with $m_b = 0$) defined as follows:

$$\Delta\frac{d\sigma}{dm_{b\bar{b}}} = \frac{d\sigma^{\text{NLO}}}{dm_{b\bar{b}}}(m_b \neq 0)$$
$$- \frac{d\sigma^{\text{NLO}}}{dm_{b\bar{b}}}(m_b = 0)\frac{d\sigma^{\text{LO}}(m_b \neq 0)}{d\sigma^{\text{LO}}(m_b = 0)}. \tag{11}$$

We notice that, in the $Zb\bar{b}$ case, finite bottom-quark mass effects are relevant up to values of the $m_{b\bar{b}}$ invariant mass around 50 GeV. Although not included in the present analysis, our calculation is still valid when both b quarks are in the forward direction. In this region, collinear singularities can arise, which are regularized by the finite b-quark mass. The resummation of the corresponding large logarithms is then appropriate and is left to future improvements.
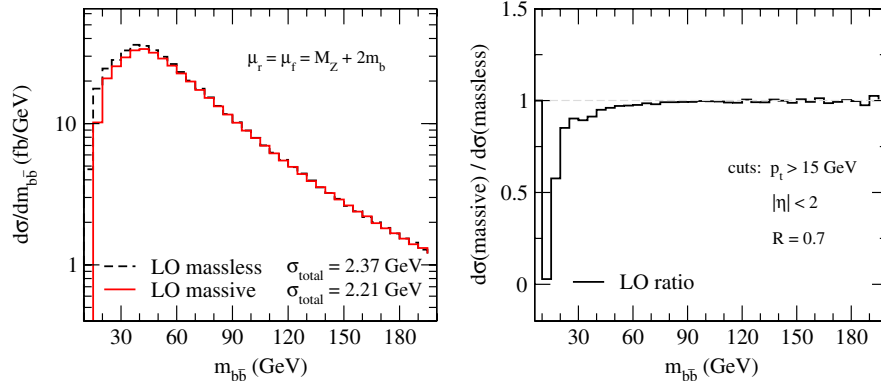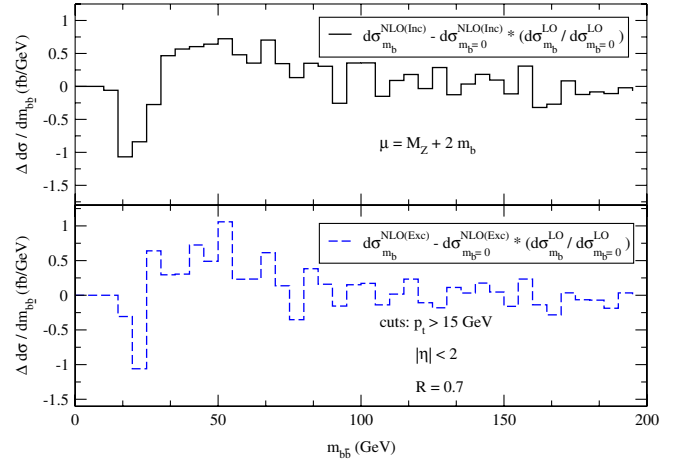

FIG. 11 (color online). The LO distribution $d\sigma/dm_{b\bar{b}}$ derived from our calculation (with $m_b \neq 0$) and from MCFM (with $m_b = 0$). The right-hand side plot shows the ratio of the two distributions, $d\sigma(m_b \neq 0)/d\sigma(m_b = 0)$.

IV. CONCLUSIONS

We have calculated the NLO QCD corrections to hadronic $Zb\bar{b}$ production including full bottom-quark mass effects. We have presented numerical results for the total cross section and the invariant mass distribution of the bottom-quark pair at the Tevatron for both massless (with MCFM) and massive bottom quarks. We apply the k_T jet algorithm, require two b-tagged jets, and impose kinematical cuts that are inspired by the D0 and CDF searches for the SM Higgs boson in ZH production. The NLO QCD $Zb\bar{b}$ cross section shows a considerably reduced renormalization and factorization scale dependence, i.e. about 20% for the *inclusive* and about 11% for the *exclusive* cross sections as opposed to a 45% scale uncertainty of the LO cross section. The bottom-quark mass effects amount to about 7% of the total NLO QCD cross section and can impact the shape of the $m_{b\bar{b}}$ distributions, in particular, in regions of low $m_{b\bar{b}}$. This is relevant to SM Higgs searches

in ZH associated production with $H \rightarrow b\bar{b}$ and to searches for MSSM Higgs bosons in $Hb\bar{b}$ production with $H \rightarrow \mu^+\mu^-$, $\tau^+\tau^-$. We also plan to apply the formalism developed in this paper to the calculation of both $Zt\bar{t}$ [68,69] and $\gamma t\bar{t}$ production at NLO in QCD. Both processes are of interest to the study of electroweak properties of the top quark [70,71], while $Zt\bar{t}$ also constitutes a relevant background to new physics searches.

ACKNOWLEDGMENTS

[1] D. E. Acosta *et al.* (CDF Collaboration), Phys. Rev. Lett. **95**, 051801 (2005).

[2] A. Abulencia *et al.* (CDF Collaboration), Phys. Rev. Lett. **96**, 081803 (2006).

[3] T. Aaltonen *et al.* (CDF Collaboration), Phys. Rev. Lett. **100**, 041801 (2008).

[4] V. M. Abazov *et al.* (D0 Collaboration), Phys. Rev. Lett. **94**, 091802 (2005).

[5] V. M. Abazov *et al.* (D0 Collaboration), Phys. Lett. B **663**, 26 (2008).

[6] V. M. Abazov *et al.* (D0 Collaboration), Phys. Lett. B **655**, 209 (2007).

[7] D. Acosta *et al.* (CDF Collaboration), Phys. Rev. D **71**, 012005 (2005).

[8] V. M. Abazov *et al.* (D0 Collaboration), Phys. Lett. B **622**, 265 (2005).

[9] CDF Collaboration, Report No. 9251, 2008.

[10] V. M. Abazov *et al.* (D0 Collaboration), Phys. Rev. D **78**, 012005 (2008).

[11] C. Kao, D. A. Dicus, R. Malhotra, and Y. Wang, Phys. Rev. D **77**, 095002 (2008).

[12] T. Han and S. Willenbrock, Phys. Lett. **273**, 167B (1991).

[13] S. Mrenna and C. P. Yuan, Phys. Lett. B **416**, 200 (1998).

[14] O. Brein, A. Djouadi, and R. Harlander, Phys. Lett. B **579**, 149 (2004).

[15] M. L. Ciccolini, S. Dittmaier, and M. Krämer, Phys. Rev. D **68**, 073003 (2003).

[16] T. Stelzer, Z. Sullivan, and S. Willenbrock, Phys. Rev. D **56**, 5919 (1997).

[17] T. Stelzer, Z. Sullivan, and S. Willenbrock, Phys. Rev. D **58**, 094021 (1998).

[18] M. C. Smith and S. Willenbrock, Phys. Rev. D **54**, 6696 (1996).

[19] B. W. Harris, E. Laenen, L. Phaf, Z. Sullivan, and S. Weinzierl, Phys. Rev. D **66**, 054024 (2002).

[20] Z. Sullivan, Phys. Rev. D **70**, 114012 (2004).

[21] Q.-H. Cao and C. P. Yuan, Phys. Rev. D **71**, 054022 (2005).

[22] Q.-H. Cao, R. Schwienhorst, and C. P. Yuan, Phys. Rev. D **71**, 054023 (2005).

[23] Q.-H. Cao, R. Schwienhorst, J. A. Benitez, R. Brock, and C. P. Yuan, Phys. Rev. D **72**, 094027 (2005).

[24] Z. Sullivan, Phys. Rev. D **72**, 094034 (2005).

[25] M. Beccaria, G. Macorini, F. M. Renard, and C. Verzegnassi, Phys. Rev. D **74**, 013008 (2006).

[26] S. Dittmaier, M. Kramer, and M. Spira, Phys. Rev. D **70**, 074010 (2004).

[27] S. Dawson, C. B. Jackson, L. Reina, and D. Wackeroth, Phys. Rev. D **69**, 074027 (2004).

[28] S. Dawson, C. B. Jackson, L. Reina, and D. Wackeroth, Phys. Rev. Lett. **94**, 031802 (2005).

[29] S. Dawson, C. B. Jackson, L. Reina, and D. Wackeroth, Int. J. Mod. Phys. A **20**, 3353 (2005).

[30] For updated results, see the CDF and D0 Web sites at http://www-cdf.fnal.gov/physics/exotic/exotic.html and http://www-d0.fnal.gov/Run2Physics/WWW/results/higgs.htm.

[31] J. Campbell and R. K. Ellis, mcfm.fnal.gov.

[32] R. K. Ellis and S. Veseli, Phys. Rev. D **60**, 011501 (1999).

[33] J. M. Campbell and R. K. Ellis, Phys. Rev. D **62**, 114012 (2000).

[34] J. Campbell and R. K. Ellis, Phys. Rev. D **65**, 113007 (2002).

[35] Z. Bern, L. J. Dixon, D. A. Kosower, and S. Weinzierl, Nucl. Phys. **B489**, 3 (1997).

[36] Z. Bern, L. J. Dixon, and D. A. Kosower, Nucl. Phys. **B513**, 3 (1998).

[37] J. Campbell, R. K. Ellis, F. Maltoni, and S. Willenbrock, Phys. Rev. D **75**, 054015 (2007).

[38] J. Campbell, R. K. Ellis, F. Maltoni, and S. Willenbrock,

Phys. Rev. D **73**, 054007 (2006).

[39] J. Campbell, R. K. Ellis, F. Febres Cordero, F. Maltoni, L. Reina, D. Wackeroth, and S. Willenbrock, arXiv:0809.3003.

[40] F. Febres Cordero, L. Reina, and D. Wackeroth, Phys. Rev. D **74**, 034007 (2006).

[41] F. Febres Cordero, L. Reina, and D. Wackeroth (work in progress).

[42] G. P. Lepage, J. Comput. Phys. **27**, 192 (1978).

[43] J. A. M. Vermaseren, arXiv:math-ph/0010025.

[44] M. Jamin and M. E. Lautenbacher, Comput. Phys. Commun. **74**, 265 (1993).

[45] G. J. van Oldenborgh and J. A. M. Vermaseren, Z. Phys. C **46**, 425 (1990).

[46] H. Murayama, I. Watanabe, and K. Hagiwara, Report No. kEK-91-11, 1992.

[47] T. Stelzer and W. F. Long, Comput. Phys. Commun. **81**, 357 (1994).

[48] F. Maltoni and T. Stelzer, J. High Energy Phys. 02 (2003) 027.

[49] L. Reina, S. Dawson, and D. Wackeroth, Phys. Rev. D **65**, 053017 (2002).

[50] S. Dawson, C. Jackson, L. H. Orr, L. Reina, and D. Wackeroth, Phys. Rev. D **68**, 034022 (2003).

[51] F. Febres Cordero, Ph.D. dissertation, Florida State University, 2007, arXiv:0809.3829.

[52] G. Passarino and M. J. G. Veltman, Nucl. Phys. **B160**, 151 (1979).

[53] A. Denner, Fortsch. Phys. **41**, 307 (1993).

[54] R. Britto, F. Cachazo, and B. Feng, Nucl. Phys. **B725**, 275 (2005).

[55] G. Ossola, C. G. Papadopoulos, and R. Pittau, Nucl. Phys. **B763**, 147 (2007).

[56] Z. Bern, L. J. Dixon, and D. A. Kosower, Phys. Lett. B **302**, 299 (1993); **318**, 649(E)(1993).

[57] Z. Bern, L. J. Dixon, and D. A. Kosower, Nucl. Phys. **B412**, 751 (1994).

[58] R. K. Ellis and G. Zanderighi, J. High Energy Phys. 02 (2008) 002.

[59] S. A. Larin, Phys. Lett. B **303**, 113 (1993).

[60] L. Bergmann, Ph.D. thesis, Florida State University, 1989.

[61] B. W. Harris and J. F. Owens, Phys. Rev. D **65**, 094032 (2002).

[62] W.-M. Yao *et al.*, J. Phys. G **33**, 31 (2006), http://pdg.lbl.gov.

[63] H. L. Lai *et al.* (CTEQ Collaboration), Eur. Phys. J. C **12**, 375 (2000).

[64] S. Catani, Y. L. Dokshitzer, and B. R. Webber, Phys. Lett. B **285**, 291 (1992).

[65] S. Catani, Y. L. Dokshitzer, M. H. Seymour, and B. R. Webber, Nucl. Phys. **B406**, 187 (1993).

[66] S. D. Ellis and D. E. Soper, Phys. Rev. D **48**, 3160 (1993).

[67] W. B. Kilgore and W. T. Giele, Phys. Rev. D **55**, 7183 (1997).

[68] A. Lazopoulos, K. Melnikov, and F. J. Petriello, Phys. Rev. D **77**, 034021 (2008).

[69] A. Lazopoulos, T. McElmurry, K. Melnikov, and F. Petriello, Phys. Lett. B **666**, 62 (2008).

[70] U. Baur, A. Juste, L. H. Orr, and D. Rainwater, Phys. Rev. D **71**, 054013 (2005).

[71] U. Baur, A. Juste, D. Rainwater, and L. H. Orr, Phys. Rev. D **73**, 034016 (2006).